Design and Demonstration of a Configurable Imaging Platform for Combined Laser, Ultrasound, and Elasticity Imaging

Heechul Yoon[#] [Student Member, IEEE],
School of Electrical and Computer Engineering, Georgia Institute of Technology, Atlanta, GA 30332 USA

Yiying I. Zhu[#],
School of Electrical and Computer Engineering, Georgia Institute of Technology, Atlanta, GA 30332 USA

Steven K. Yarmoska [Student Member, IEEE],
U.S. National Institutes of Health under fellowship grant CA216939 and is with the Wallace H. Coulter Department of Biomedical Engineering, Georgia Institute of Technology and Emory University School of Medicine, Atlanta, GA 30332 USA

Stanislav Y. Emelianov [Senior Member, IEEE]
School of Electrical and Computer Engineering, Georgia Institute of Technology, Atlanta, GA 30332 USA and with the Wallace H. Coulter Department of Biomedical Engineering, Georgia Institute of Technology and Emory University School of Medicine, Atlanta, GA 30332 USA

[#] These authors contributed equally to this work.

Abstract

This paper introduces a configurable combined laser, ultrasound, and elasticity (CLUE) imaging platform. The CLUE platform enables imaging sequences capable of simultaneously providing quantitative acoustic, optical, and mechanical contrast for comprehensive diagnosis and monitoring of complex diseases, such as cancer. The CLUE imaging platform was developed on a Verasonics ultrasound scanner integrated with a pulsed laser, and it was designed to be modular and scalable to allow researchers to create their own specific imaging sequences efficiently. The CLUE imaging platform and sequence were demonstrated in a tissue-mimicking phantom containing a stiff inclusion labeled with optically-activated nanodroplets and in an ex vivo mouse spleen. We have shown that CLUE imaging can simultaneously capture multi-functional imaging signals providing quantitative information on tissue.

Keywords

Cancer diagnosis; combined imaging platform; optically-triggered nanodroplets; photoacoustic imaging; shearwave elasticity imaging; ultrasound imaging

Corresponding author: Stanislav Y. Emelianov: stas@gatech.edu.

I. INTRODUCTION

AS cancer progresses, it undergoes complex pathological and biological changes that significantly vary from person to person. Thus, precise diagnosis and personalized treatment of cancer necessitates a variety of information on its morphology, functionality, molecular composition, and bio-mechanics [1, 2]. It is desirable to gauge all of these various aspects of cancer to improve its detection, staging, treatment, and management [3]. However, none of the currently used stand-alone biomedical imaging modalities provides this broad information on cancer, which has led to the development of hybrid or multi-modal approaches [3, 4]. For example, a combination of positron emission tomography (PET) and computed tomography (CT) referred to as PET/CT synergistically complement each other, as PET offers metabolic contrast that can be superimposed on the superior anatomical visualization of CT. The synergy of PET/CT produced a more accurate and widely-used diagnostic modality for cancer staging and management. However, nuclear medicine-based imaging techniques are encumbered by their reliance on ionizing radioisotopes for contrast [3].

Ultrasound (US) is a safe, noninvasive, real-time, portable, and cost-effective imaging modality. Thus, as a first-line screening tool, US imaging has been widely used in the clinic to aid detection of cancers, such as breast, liver, thyroid, prostate cancer and others [5–7]. However, its sensitivity and specificity to tumors are relatively low compared to other imaging modalities, as the acoustic properties of a tumor and its surrounding tissue are similar [5]. Furthermore, US imaging is often operator dependent and therefore not always objective [8]. To address these limitations, various ultrasoundbased imaging methods, including shear-wave elasticity imaging (SWEI), spectroscopic photoacoustic (sPA) imaging, and contrast-enhanced US imaging, have been rigorously investigated.

First, SWEI can quantify elastic properties of tissue non-invasively. As the pathological condition of cancer is closely related to its stiffness in many solid lesions, SWEI has shown great potential in differentiating benign and malignant tumors [9–11]. In principle, SWEI relies on shear waves generated by the application of acoustic radiation force (ARF). The propagation of the shear waves is then observed by high-framerate ultrasound imaging to estimate their velocity, denoted as a shear-wave velocity (SWV) that is associated with the shear modulus of tissue. Since SWEI was introduced [12], various SWEI-based methods have been an active area of research [13–16]. Moreover, SWEI has been applied to several clinical applications, showing promising capabilities in cancer diagnosis and monitoring [9, 17].

Integrating a laser with an ultrasound system enables photoacoustic (PA) imaging, which offers optical contrast from endogenous and/or exogenous absorbers in tissue based on the PA effect, creating acoustic signals in response to pulsed-laser irradiation and subsequent thermal expansion [18, 19]. For example, hemoglobin in blood is a strong absorber, providing adequate PA signals compared to surrounding chromophores; thus, hemoglobin contrast from PA has been used to identify the formation of vessels surrounding a tumor, as the structural complexity of tumor neovasculature is often an indicator of tumor malignancy [20]. Furthermore, the level of blood oxygen saturation (SO_2), the ratio of oxygenated to

total hemoglobin concentrations, is highly associated with the pathological state of a tumor [21, 22]. Malignant tumors and metastatic sentinel lymph nodes have been shown to have a lower level of SO_2 compared to normal tissue [23–26].

Contrast-enhanced ultrasound imaging relying on clinicallyapproved contrast agents (i.e., microbubbles) has been widely used in the clinic, as it provides superior contrast over traditional gay-scale US images [27, 28]. To separate microbubbles from surrounding tissue in US imaging, pulse inversion-based methods, capturing microbubbles' unique nonlinear response, are typically used. Recently, to further expand the utility of microbubbles, submicrometer-sized phase-change contrast agents have been recently introduced [29–31]. These agents (typically, perfluorocarbon nanodroplets) can form microbubbles *in situ* in response to an acoustic or optical trigger [30, 32]. Because of their submicrometer size, they have the potential to extravasate from endothelial fenestrations in cancer neovasculature and are thus capable of imaging extravascular targets. Our group and others have focused on optically-triggered perfluorohexane nanodroplets (PFHnDs) that can repeatedly vaporize and recondense, providing repeatable high-contrast PA and ΔUS signals [31, 33, 34]. These agents have shown great potential in contrast-enhanced imaging and super-resolution imaging for lymph node localization and brain vasculature mapping. High-frame-rate US imaging is typically required to capture the temporal response of the PFHnDs, because their vaporization and recondensation process is transient and stochastic [35].

Previously, we have introduced combined multi-wavelength photoacoustic and plane-wave ultrasound (mwPA/pwUS) imaging that can trigger laser pulses with multiple optical wavelengths to support sPA imaging and activate the PFHnD; it allows for observation of transient PFHnD dynamics activated at various optical wavelengths with ultrafast US imaging [36]. The mwPA/pwUS imaging has shown its promising ability to capture acoustic and optical contrast of PFHnDs as a function of both time and optical wavelength, but it lacks an ability to measure the mechanical properties of tissue. To address this issue, there were a few attempts combining ultrasound, photoacoustic, and elasticity imaging. Emelianov *et al.* combined ultrasound, strain, and photoacoustic imaging [37]. However, their strain imaging could not offer quantitative mechanical properties of tissue and PA imaging with single-wavelength does not quantify the concentration of chromophores. More recently, Nguyen *et al.* replaced strain imaging by quantitative SWEI and added thermal strain imaging, quantifying lipid-based tissue composition [38]. However, their PA imaging remains qualitative, and their system does not support mwPA/pwUS imaging.

This paper introduces a configurable, module-based imaging platform, referred to as the combined laser, ultrasound, and elasticity (CLUE) imaging platform. The CLUE imaging platform is capable of supporting various imaging sequences for general researchers in this field to explore a wide array of clinical applications. In the design of the imaging platform, we define each imaging function as a "module," and we allow users to allocate these imaging modules arbitrarily to design their own custom imaging sequences according to their specific needs. Currently, we introduce 14 imaging modules including pulsed-laser excitation, ultrafast US acquisition, and ARF application. These imaging modules can be freely placed as a series of imaging functions when designing an imaging sequence. We have developed the CLUE imaging platform using a specific ultrasound research scanner and

laser system, but our design philosophy can be adapted to other hardware. Our CLUE imaging platform and relevant graphical user interface (GUI) scripts are shared in a script repository in the Verasonics Community (http://verasonicscommunity.com). Furthermore, this paper introduces a representative imaging sequence referred to as a CLUE imaging sequence that acquires all ultrasound-based quantitative mechanical and functional information on tissue using SWEI and PA and ultrafast US imaging with laser-activated PFHnDs. Because the CLUE imaging sequence can assess multiple quantitative aspects of tissue simultaneously, it potentially can be used to comprehensively characterize the prognosis and treatment response of diseases, such as cancer.

In this paper, we first introduce a system configuration consisting of an ultrasound system and a laser, and then we explain design details of the developed CLUE imaging platform. Next, we present a representative CLUE imaging sequence, designed on the CLUE imaging platform. To demonstrate this imaging sequence on the CLUE imaging platform, experimental methods for phantom and *ex vivo* mouse spleen imaging studies are described. Subsequent imaging results and discussion follow.

II. DESIGN OF CONFIGURABLE IMAGING PLATFORM

A. A Set-Up for Laser and Ultrasound Systems

Our configurable CLUE imaging platform was developed on a programmable ultrasound research scanner (Vantage 256™; Verasonics, Inc., Kirkland, WA, USA) integrated with a tunable pulsed laser (Phocus Mobile; Opotek Inc., Carlsbad, CA, USA) as illustrated in Fig. 1. Note that although the Phocus Mobile laser was used, other laser systems are not excluded, as typical laser systems have a similar communication protocol. In addition, the CLUE imaging platform was designed on the Verasonics scanner, but the same design approach could be applied to other ultrasound imaging systems.

In our setup, the laser and the Verasonics system communicate in the following order: (1) A periodic Flashlamp OUT signal from the laser triggers the Verasonics system through Trig IN1 to indicate the laser is ready to fire, and then, (2) once triggered, the Verasonics system sends a Trig OUT signal to the laser through a function generator to fire an actual laser pulse after a pre-determined Q-Switch delay. Here, a Q-Switch delay is a delay time between the Flashlamp OUT signal and the Q-Switch IN signal controlled by the Verasonics system, and it determines the energy of a laser pulse. In general, a longer Q-Switch delay makes the output energy of the laser weaker. When delivering the Trig OUT signal from the Verasonics system to the Q-Switch IN of the laser, the function generator is used to invert the phase and to extend the duration of the Trig OUT signal in order to satisfy the input requirements of the Phocus laser. This laser requires an input trigger to be positive and last for 50 μs, but the Verasonics outputs a negative signal of 1-μs duration. The same approach can also be found from our previous study [36]. Additionally, a laser energy meter (Pulsar-2; Ophir Optronics Solutions, Inc., Jerusalem, Israel) placed inside the laser was used to measure and collect the energy of irradiated laser pulses.

There are two more potential setups that may be equipped in the current system configuration: a photodetector and an external transducer setup in Fig. 1. In the case that the

time delay between the Trig OUT signal (i.e., Q-Switch IN) and the actual laser pulse is not negligible, which may introduce an undesirable delay in PA imaging, a photodetector is potentially incorporated to synchronize PA imaging. As the photodetector can output a trigger once it senses pulsed-laser irradiation, this trigger can be input to the Verasonics system through the second trigger input (Trig IN2) for exact synchronization between actual firing of the laser pulse and reception timing of PA signals. In addition, in the case that an external transducer is used for ARF application, the Trig OUT signal can be potentially used to control a setup for the external transducer, instead of the pulsed laser.

B. Module-based Configurable Imaging Platform

The overall process of imaging sequence design and execution using our imaging platform, referred to as the "CLUE imaging platform," is illustrated in Fig. 2. The 14 imaging modules listed in Table I are shown on top of Fig. 2. The crux of the CLUE imaging platform is that it allows users to design any customized imaging sequence by flexible, serial allocation of "imaging modules" and selection of relevant imaging parameters according to their specific need, as shown in Fig. 2. Based on the designed imaging sequence, the CLUE imaging platform scalably generates all relevant Verasonics objects that are required to run the system, regardless of the number of imaging modules used in the sequence, as long as the system memory supports the amount of data to be loaded.

The imaging modules consist of 14 fundamental building blocks of the imaging sequence, as defined in Table I. UF (ultrafast) represents ultrafast ultrasound imaging, which acquires a full two-dimensional image with plane-wave compounding, and LL (line-by-line) ray-based ultrasound imaging that sequentially acquires each scanline per transmit-receive event with a focused beam [39]. The UF and LL modules can be extended with either PI (pulse inversion) or INTL (interleaving) or both. PI supports pulse-inversion-based harmonic imaging. Here, PI uses two pulses with opposite phases (i.e., positive and negative). INTL enables multiple acquisition with different transmit offset times to increase the effective sampling rate for high-frequency ultrasound imaging. For example, since the maximum sampling rate of the Verasonics system is 62.5 MHz, two interleaved acquisitions can make the effective sample rate 125 MHz, supporting an effectively doubled center frequency. Note that currently, only the Vantage Verasonics systems configured with the "high-frequency" option support this interleaved sampling approach. Also, INTL-related modules are unavailable in the current platform, but will be supported in future updates. The PA module only receives the signals, and thus, it usually necessitates a preceding ExtLaser (external laser) module, which irradiates a laser pulse to generate the photoacoustic signals. Nevertheless, the PA and ExtLaser modules are designed to be independent like other modules. Hence, either one of them can be used independently according to the study purpose. The IntARF (internal ARF) and ExtARF (external ARF) modules are to apply an ARF to create shear waves for SWEI. Here, for ARF excitation, the IntARF module uses an imaging transducer connected to the Verasonics system, but the ExtARF module triggers an external transducer or a mechanical excitation source. The Doppler module acquires both color and power Doppler images for flow quantification. The Idle module creates an idle wait step for a user-specified time duration to control the acquisition timings between other modules. These fundamental modules can be used to create various imaging sequences. Specifically, in the CLUE

platform script, there is an array that a user can serially place any imaging modules to be used for their data acquisition sequence. For example, a simple US/PA imaging sequence can be designed with a series of the UF (or LL), ExtLaser, and PA modules.

The CLUE imaging platform offers three default realtime imaging methods: US, US/PA, and US/Doppler imaging modes. A user can switch to any of these three modes in a Verasonics GUI. A button was created on the GUI to execute the user-designed custom imaging sequence. Real-time imaging will be paused when the data acquisition is in process. Once data is acquired and saved for offline processing, realtime imaging will resume. In Fig. 2, a representative imaging sequence is shown. First, a sham laser pulse is placed at the beginning for synchronization of the US system and the laser. Because the timing of pulsed-laser irradiation is determined by periodic Flashlamp OUT triggers of the laser, the sham laser pulse allows the sequence to expect an irradiated timing of the next actual laser pulse, enabling acquisition of US images exactly prior to the actual laser excitation. Specifically, the pulse-repetition frequency (PRF) of the Flashlamp OUT signal is constant at 10 Hz in the Phocus laser (i.e., pulserepetition interval (PRI) of 100 ms). Thus, the Idle module with an appropriate duration can be inserted right after the irradiation of the sham laser pulse specified by the ExtLaser module. For example, if pre-laser US imaging is to acquire 50 frames at 10 kHz, it will take 5 ms for data acquisition. Thus, 95 ms (= 100 ms (laser PRI) – 5 ms (pre-laser US acquisition)) of the Idle module duration is needed to enable the pre-laser US acquisition right before the actual laser pulse. Following the laser irradiation, corresponding PA and postlaser US images are captured in the imaging sequence. Then, two SWEI processes are executed, where each process consists of two modules: an IntARF module for ARF application and a subsequent UF module for shear wave observation. Here, two IntARF modules in two SWEI processes apply the ARF beams at different lateral positions to cover a complete view of SWEI mapping. The Idle module between two SWEI acquisitions is to ensure the safety limits outlined by the Food and Drug Administration [40].

C. Interface of CLUE Imaging Platform

Verasonics systems are one of the most widely used research ultrasound scanners in a diverse array of applications: from nondestructive evaluation (NDE) to clinical diagnosis (http://verasonics.com/scientific-references/). A user can design and use their imaging sequence by defining Verasonics objects in the MATLAB (MathWorks, Natick, MA) environment. The Verasonics objects are classified in two groups: global system objects and sequence objects. The global system objects (Resource, Trans, and PData) define system specifications, medium properties, and transducer characteristics. The sequence objects (TW, TX, TPC, Receive, Recon, ReconInfo, Process, Event, and SeqControl) determine a sequence of imaging, image reconstruction, and image display. Thus, as shown in the left part of Fig. 3, a user is required to define all Verasonics objects to run their script on the system (various example scripts and a detailed user manual are provided with the system).

The CLUE imaging platform is a module-based configurable imaging platform, providing non-advanced users a shortcut to sophisticated imaging sequences. As shown in the right part of Fig. 3, the CLUE imaging platform interfaces Verasonics software and hardware on

behalf of a user, and thus, one only needs to define their imaging sequence by allocating the imaging modules listed in Table I. All objects required in the Verasonics programming script are generated by our platform automatically. Once the imaging sequence is defined, relevant parameters per imaging module can be set in the script or through a custom-made GUI. Then, the CLUE imaging platform creates the corresponding Verasonics objects scalably according to the designed imaging modules with the determined parameters.

III. EXPERIMENTAL METHODS AND MATERIALS

A. Combined Laser, Ultrasound, and Elasticity (CLUE) Imaging

To demonstrate the integrated implementation of various ultrasound-based imaging modules, our CLUE imaging sequence includes ultrafast US imaging, PA imaging, and SWEI. The combination of the first two are to detect the PFHnDs, which can be used for contrast-enhanced or super-resolution imaging [33–35]. The PFHnDs vaporize and recondense in response to pulsed-laser irradiation and their transient response requires high-frame-rate US imaging [35]. In addition, the vaporization event also provides strong PA signals. Thus, in the CLUE imaging sequence shown in Fig. 4, we used two respective UF imaging modules before and after laser pulses to capture the dynamic response of the PFHnDs (blue rectangle). The differential US (US) image, which is obtained by subtracting pre- and post-laser US images, is used to visualize the vaporized PFHnDs. We repeated this process 5 times with increasing optical fluence. Thereafter, three SWEI sequences with three ARFs applied at different lateral positions (left/right/middle) follow (red rectangle). The propagation of shear waves was visualized through a two-dimensional autocorrelation approach [41] and these shear waves were used to reconstruct the corresponding SWV maps using a two-dimensional cross-correlation approach [42]. Overall, IQ data generated from all imaging modules were saved immediately after acquisition, and the result images were processed offline.

This study used a linear array ultrasound transducer (CL157; Philips Healthcare, Andover, MA, USA). Table II lists all parameters used in the CLUE imaging sequence. Laser pulsing was repeatedly disabled and enabled to obtain pre-laser US images immediately prior to the actual laser pulse (for example, UF 1 is placed before ExtLaser 2 in Fig. 4). Thus, the Idle module was used to control the acquisition time. The desired duration of the Idle module was computed by subtracting a QSwitch delay and a pre-laser US acquisition duration from the laser PRI (100 ms). Immediately after irradiating a laser pulse, PA imaging and subsequent post-laser US imaging followed. This study applied 5 actual laser pulses as a function of QSwitch delay to demonstrate its ability to adjust the optical fluence with respect to laser pulse, which allows for evaluation of the optical vaporization threshold of the PFHnDs. The Q-Switch delay decreased with each successive laser pulse (400, 350, 300, 270, 250 μs), increasing the irradiated optical fluence accordingly. The average measured fluence values at the output of the optical fiber bundles were 33, 54, 77, 90, and 94 mJ/cm^2.

SWEI in the CLUE imaging sequence consisted of three ARF applications and three ultrafast ultrasound acquisitions to obtain the mechanical properties of tissue. As listed in Table II, the ARFs were applied at three lateral locations and the propagation of the shear waves were respectively tracked at a PRF of 10 kHz. Three angles of plane waves were used

for angular compounding [39]. For the ARF beams, f-number of 2.5, a focal depth of 17.5 mm, a pulse duration of 200 μs, and a center frequency of 6.5 MHz were used. Between pushing and tracking events, an interval of 500 ms was placed using the Idle module.

B. Synthesis of Perfluorohexane Nanodroplets (PFHnDs)

Perfluorohexane nanodroplets were synthesized using a sonication-based protocol. Briefly, 1 μmol of DSPC and DSPE-mPEG2000 in a 1:9 molar ratio were isolated along with 0.5 mg of near-infrared-absorbing dye (IR-1048; SigmaAldrich) from a chloroform solution using a rotary evaporator. After rotary evaporation produced an even cake of lipid and dye, the solid isolate was further dried under nitrogen flow in order to evaporator all residual chloroform.

Next, the solid reagents were hydrated with 1 mL of 7.40 pH PBS and agitated using a water bath sonicator to produce a solution of dye-loaded nanomicelles. This solution was centrifuged at 300 rcf for 1 minute in order to pellet excess near-infrared dye. Then, 900 μL of the nanomicelle-containing supernatant was combined with 100 μL of PBS and 50 μL of perfluorohexane. This solution was then probe sonicated (1s on, 15s off, 5 times) on ice in order to produce a stock solution of PFHnDs.

Prior to their use for imaging, 100 μL of PFHnDs were diluted in 2 mL of PBS and bath sonicated for 5 minutes. This solution would then be centrifuged at 3000 rcf for 5 minutes in order to pellet PFHnDs. The supernatant would then be removed and the PFHnDs would be reconstituted in 100 μL of sterile saline for imaging. This protocol produces PFHnDs with an average hydrodynamic diameter of 222 nm measured via dynamic light scattering (Zetasizer Nano ZS; Malvern Instruments Ltd.) and at a concentration of approximately 10^{10} PFHnDs/mL as assessed by nanoparticle tracking analysis (NanoSight NS300; Malvern Panalytical).

C. Tissue-Mimicking Phantom Synthesis and Imaging

A tissue-mimicking gelatin phantom containing a cylindrical stiff inclusion labeled with the synthesized PFHnDs was fabricated to demonstrate the CLUE imaging sequence. The diameter of the inclusion was 7 mm. The concentrations of the gelatin powders in the inclusion and background were 12% w/v and 6% w/v, respectively. Thus, a SWV ratio of the inclusion to the background was expected to be two, as the stiffness of a gelatin phantom is proportional to its gelatin concentration. The v/v ratio of the as-prepared PFHnDs solution to the inclusion was 1:1000. For acoustic scattering, 0.5% w/v silica particles were included both in the inclusion and in the background. The imaging depth of the center of the inclusion was approximately 17.5 mm. The CLUE imaging sequence was repeated three times to evaluate means and standard deviations (SDs) of the pre-laser US, PA, post-laser US, US, and SWV images over independent measurement.

D. Mouse Spleen Preparation for Ex Vivo Imaging

All animal procedures were performed under the oversight of the Institutional Animal Care and Use Committee at the Georgia Institute of Technology. For *ex vivo* spleen imaging, an 18-week-old female athymic nude mouse (NU/J; The Jackson Laboratory) was placed under general anesthesia with isoflurane (5% induction, 2.5% maintenance; 0.5 L/min O$_2$) and

injected via the jugular vein with 140 μL of 10^{10} PFHnD/mL particles, prepared as described in section "B." After injection, the mouse was returned to consciousness and kept in the Animal Resources Facility at Georgia Tech for 24 hours. This time allows for injected particles to be filtered within splenic sinusoids and endocytosed by resident reticuloendothelial cells. After 24 hours, the mouse was humanely euthanized by an intraperitoneal lethal injection of Euthasol (Sodium pentobarbital 390 mg/ml, 150 mg/kg; Henry Schein Medical). Following cessation of the heartbeat, euthanasia was confirmed by secondary cervical dislocation. Immediately after secondary euthanasia, the spleen was dissected and kept submerged in 6.80 pH-buffered PBS solution prior to phantom inclusion.

Within two hours post-resection, the mouse spleen was immediately embedded in a gelatin phantom to fix its movement and improve the acoustic coupling. Then, the mouse spleen was imaged using the same CLUE imaging sequence as described previously in Section III. A.

IV.   RESULTS AND DISCUSSION

A.   CLUE Imaging of a Phantom Containing a Stiff Inclusion

The CLUE imaging sequence introduced in Fig. 4 was applied to the gelatin phantom containing a stiff cylindrical inclusion. Fig. 5 shows the corresponding pre-laser US, PA, post-laser US, and US images as a function of laser pulse. At the lowest fluence (i.e., 33 mJ/cm^2) in Fig. 6 (a) and (p), almost no PA and ΔUS signals were detectable, and thus, we conclude that the laser pulse at this fluence level did not activate the PFHnDs. As optical fluence increased from 33 mJ/cm^2 to 94 mJ/cm^2, the number of triggered PFHnDs increased, resulting in the growing PA and ΔUS signals. However, in pre- and post-laser B-scan US images (the first and third row images), no obvious differences were observable. This is because the signals coming from the vaporized PFHnDs were relatively subtle compared to those from other acoustic scatters in the phantom. Thus, taking a difference between pre- and post-laser US images (i.e., US images) shown in the fourth row (Fig. 5 (p), (q), (r), (s), and (t)) could be useful in identifying the optical activation of the PFHnDs for high-contrast imaging.

Means and SDs of the PA signals in the stiff inclusion (region-of-interest for the inclusion is circled with a white dotted line in Fig. 5 (a)) and in the background region were computed with three measurements as shown in Fig. 6. The background mean PA signals did not change significantly with respect to optical fluence and were consistently negligible (gray dotted line), but the PFHnDs contained in the inclusion resulted in increasing mean PA signals (black solid line). As the vaporization process is a combined, complex function of various factors including droplet size, local fluence, amount of dye encapsulated, and local temperature [35], the PFHnDs vaporize stochastically. Thus, the vaporization threshold is unique to each formulation. Therefore, the increase in the mean PA signal resulting from the expansion of the PFHnDs is not completely discrete as shown in Fig. 6.

ΔUS images removing background signals showed the vaporized PFHnDs with high contrast (fourth row images in Fig. 5). Means and SDs of ΔUS signals inside and outside of the inclusion were computed and plotted in Fig. 7. Like the results observed in Fig. 6, the mean

ΔUS signals in the background (gray dotted line) do not change as a function of fluence, but those in the inclusion (black solid line) increased as optical fluence increased, which vaporized more PFHnDs.

In addition, the background US signals in Fig. 7 showed higher SDs than the background PA signals in Fig. 6, which may be due to the subtraction of two images to form the ΔUS images. Subtracting two pre- and post-activation images is the same as two-tap high-pass filtering, which likely increases high-frequency noise components in the image. Thus, the SDs of the background ΔUS signals could be larger than those of the background PA signals for the same vaporization phenomena.

Furthermore, ΔUS signals could be undesirably increased when two successive images have motion in-between, which may have introduced unnaturally high SD in the ΔUS signals both in the background and the inclusion at 94 mJ/cm^2 (Fig. 7). Correspondingly, it was observed in Fig. 5 (t) that the background and inclusion ΔUS signals are higher than expected. Lastly, as the means and the SDs were measured three times and the vaporization process of PFHnDs is stochastic, the overall means and SDs in PA and ΔUS signals may not be always consistent as a function of optical fluence.

On the same target, the CLUE imaging sequence obtained the SWEI results as shown in Fig. 8. We applied three ARF beams at different lateral locations (−7 mm, +7 mm, and 0 mm) and observed the corresponding generation and propagation of the shear waves. Three rows in Fig. 8 represent three lateral locations of ARF application. As the shear waves propagate through the stiff region, they became faster, as observed in the axial velocity sequences at multiple downstream time points (the second to fifth column images in Fig. 8). Here, note that the time interval between the last laser pulse firing and the beginning of shear wave tracking (μ10.5 ms) was long enough for the PFHnDs in the inclusion to recondense back to their original liquid state. As such, the propagation of shear waves through the inclusion would not be impeded by residual microbubbles. The respective SWV maps reconstructed from each axial velocity sequence are shown in Fig. 8 (f), (l), and (r). On the regions where the push beams were applied, the propagation of the shear waves is not observable. Therefore, the SWVs on the pushing regions are unreliable. This limitation typically requires multiple applications of ARF beams at different lateral locations to span the full field-of-view while still omitting unwanted regions in the SWV map prior to combining multiple SWV maps. The combined SWV map from the three acquired SWV maps is given in Fig. 8 (s). The inclusion center was placed at 17.5 mm in depth. We found that mean SWVs inside and outside of the inclusion were 4.22 m/s, and 2.81 m/s, respectively. Thus, the corresponding Young's moduli are 53.43 kPa and 23.69 kPa, with the assumption that the density of the phantom is 1,000 kg/m^3. Here, the ratio of the estimated Young's moduli (i.e., 53.43 kPa / 23.69 kPa = 2.26) is close to the ratio of the gelatin concentration of the inclusion to that of the background (i.e., 12% / 6% = 2), which may indicate that our SWV measurement is valid [43].

Overall, we have demonstrated that the CLUE imaging can sense multiple properties of the imaging target simultaneously through our gelatin phantom study. The stiff PFHnD-labeled inclusion offered both the laser-induced contrast by PA and ΔUS imaging and mechanical

contrast by SWEI. Note that because the ΔUS images were taken between pre- and postactivation of the PFHnDs, the corresponding information (or contrast) resulting from the vaporization of PFHnDs is similar to standard PA contrast. However, endogenous photoabsorbers, including hemoglobin and lipid, would produce background PA signals, whereas ΔUS removes the background, and retains the signals from PFHnDs only. Furthermore, additional information from the PFHnDs can be potentially obtained, if temporal ΔUS images during the recondensation of the PFHnDs are analyzed. For example, our previous studies have shown that it can facilitate various imaging methods, including super-resolution imaging [33, 35].

B. CLUE imaging of Ex Vivo Spleen

To further demonstrate the feasibility of CLUE imaging, we imaged a cross-section of an *ex vivo* mouse spleen embedded in a homogeneous gelatin background as shown in Fig. 9.

Similar to the gelatin inclusion study introduced in the previous section, no overt differences between pre- and postlaser US images can be observed over increasing optical fluences. However, we could confirm that the intravenously injected PFHnDs successfully accumulated in the spleen before extraction. Therefore, similar to the phantom case, the PA and ΔUS signals inside the spleen increased due to the increased vaporization of PFHnDs as a function of optical fluence. However, note that the ΔUS signals in Fig. 9 (p) seem to be stronger than those obtained with higher optical fluences in Fig. 9 (q) and Fig. 9 (r). This may be due to subtle motion/perturbation that occurred during the data acquisition. For this reason, US images between pre- and post-activation of PFHnDs do not always contain only the PFHnD signals. To ensure that a vaporization event occurred, the PA images need to be compared with corresponding US images during the recondensation phase [36]. In addition, the artificial lines in the PA images in Fig. 9 are PA reverberation artifacts resulting from the PA signal generated from the surface of the transducer.

From the estimated axial velocity sequences in Fig. 10, it is observed that shear waves were successfully created and propagated through the spleen. As shown in Fig. 10, the spleen seemed to be stiffer than the gelatin background, which resulted in faster SWVs propagating through the spleen. Three SWV maps acquired at three lateral positions were again reconstructed from the corresponding axial velocity sequences, but there is a noticeable difference in the SWVs in the spleen between Fig. 10 (f) and (l). This is possibly due to the unexpected broadening of shear waves [44], as the spleen is not ideally cylindrical, which might have led to the wider (or more blurred) shear wave front in Fig. 10 (e) than that in Fig. 10 (k). A combined SWV map is presented Fig. 10 (s).

C. Potential Limitations and Utilities of CLUE Imaging

CLUE imaging may not be able to always capture all mechanical, optical, acoustic information in soft tissue. One of the most critical concerns would be a limitation in light penetration. Because of optical absorption and scattering, pulsedlaser light becomes diffuse in biological tissue. Although nearinfrared light can reach depths at several centimeters, PA imaging of deep tissue is still challenging [45]. Furthermore, sPA imaging of chromophore concentrations gets significantly inaccurate as the imaging target goes deeper or the PA

signalto-noise ratio gets lower [46]. On the other hand, SWEI relies on the ARF application to generate and thus to monitor shear waves. However, because of the attenuation of shear waves, adequate generation of shear waves is desired [13, 15, 16]. In addition, the generation of shear waves is highly dependent on the regional characteristics of tissue, such as, coupling stress resulting from internal organs, boundary conditions, and viscoelasticity [47]. In general, SWEI has many parameters to be optimized for successful execution. For example, the spatial resolution of SWEI is mainly determined by the kernel size used in estimating the SWV and the shear wavelength [44, 48]. Moreover, in a clinical setting, the frequency of ARF application is limited in SWEI by the FDA-imposed safety limit. Multiple acquisitions of SWEI may introduce motion artifacts resulting from physiological motion such as pulsation, respiration, and cardiac activity [49]. The frequency of laser irradiation is limited by the safety guidance and also by the flashlamp, which may introduce the same motion artifacts in PA and ΔUS imaging of the PFHnDs. Thus, given these challenges in PA imaging and SWEI, CLUE imaging could be partially functional in a region of interest dependent upon depth and local tissue properties. In other words, a region of interest, where PA imaging is insensitive, can rely on SWEI and vice versa.

CLUE imaging has promising potential in various clinical applications. Not only does CLUE imaging help to understand progress, status, and prognosis of disease, but also it can be a valuable tool for therapeutic guidance. Currently, assessment of a treatment response of cancer is likely delayed, as monitoring the reduction of the tumor size is used as a standard method [50]. Thus, it may be beneficial to apply CLUE imaging to monitor the changes in both mechanical and functional properties of cancer in response to specific therapy, as it can provide immediate and collective information on treatment progress. For example, sPA imaging and SWEI have shown their respective capabilities in evaluating various therapeutic approaches [17, 50, 51]. Monitoring oxygenation of a tumor for effective therapeutic radiation sensitization and promptly evaluating its response to radiation would be feasible using sPA imaging and SWEI, respectively, which would be simultaneously possible through CLUE imaging.

This study used a linear array transducer and bifurcated optical fiber bundles to demonstrate the CLUE imaging platform. However, as the Verasonics system supports custom-made transducers, various types of transducers and different ways of light delivery can be potentially incorporated with our platform to further expand its utility. For example, a handheld concave or multi-segment ultrasound array transducer with a partial or full field-of-view can be utilized for PA tomographic imaging in the clinical setting [52, 53]. Furthermore, three-dimensional (3-D) US/PA imaging might also be desired, but it demands extensive hardware and computational complexity. One group attempted to address this issue via passive ultrasound generation with an optical absorber [54]. This study showed promising potential for fast 3-D US/PA imaging, which may be adapted to the CLUE imaging platform, as they used the same number of transducer elements. Moreover, for monitoring of photothermal therapy and ablation, 3-D PA-based temperature mapping was demonstrated with a 512-element two-dimensional (2-D) spherical array transducer [55]. Such configuration can be implemented using the CLUE imaging platform. However, note that the number of array elements is limited in the Verasonics system (256 channels are available in our Vantage-256™ system), but can be expanded up to 2,048 channels by

synchronization of multiple systems. Overall, the CLUE imaging platform does not necessarily restrict the type of US/PA transducers or method of light illumination, and various 2-D and 3-D imaging approaches can be supported based on user needs.

V. CONCLUSION

We have introduced and designed the CLUE imaging platform and sequence as a research tool for comprehensive diagnosis of complex disease. Furthermore, the development of the CLUE imaging platform will also support imaging studies for ultrasound researchers in a wide array of disease applications. In our module-configurable, scalable CLUE platform, an arbitrary imaging sequence can be created by allocating pre-defined imaging modules. To demonstrate the developed CLUE imaging platform in the tissue-mimicking gelatin phantom and the *ex vivo* mouse spleen, we have applied a representative CLUE imaging sequence, which can acquire pre-laser US, PA, post-laser US, and SWV images. The imaging results collectively showed multiple desired imaging contrast—acoustic, optical, and mechanical— from both the PFHnD-labeled stiff inclusion and the PFHnD-laden spleen, suggesting that the introduced CLUE imaging platform and sequence can be potentially used to provide comprehensive soft tissue assessment.

REFERENCES

[1]. Hanahan D and Weinberg Robert A., "Hallmarks of Cancer: The Next Generation," Cell, vol. 144, pp. 646–674, 2011. [PubMed: 21376230]

[2]. Alizadeh AA, Aranda V, Bardelli A, Blanpain C, Bock C, Borowski C, Caldas C, Califano A, Doherty M, Elsner M, et al., "Toward understanding and exploiting tumor heterogeneity," Nat. Med, vol. 21, pp. 846–853, 2015. [PubMed: 26248267]

[3]. Fass L, "Imaging and cancer: A review," Mol. Oncol,, vol. 2, pp. 115152, 2008.

[4]. Tempany C, Jayender J, Kapur T, Bueno R, Golby A, Agar N, and Jolesz F, "Multimodal Imaging for Improved Diagnosis and Treatment of Cancers," Cancer, vol. 121, pp. 817–827, 2015. [PubMed: 25204551]

[5]. Guo R, Lu G, Qin B, and Fei B, "Ultrasound Imaging Technologies for Breast Cancer Detection and Management: A Review," Ultrasound Med. Biol, vol. 44, pp. 37–70, 2018. [PubMed: 29107353]

[6]. Ariff B, Lloyd CR, Khan S, Shariff M, Thillainayagam AV, Bansi DS, Khan SA, Taylor-Robinson SD, and Lim AKP, "Imaging of liver cancer," World J. Gastroenterol, vol. 15, pp. 1289–1300, 2009. [PubMed: 19294758]

[7]. Xie C, Cox P, Taylor N, and LaPorte S, "Ultrasonography of thyroid nodules: a pictorial review," Insights Imaging, vol. 7, pp. 77–86, 2016. [PubMed: 26611469]

[8]. Hooley RJ, Scoutt LM, and Philpotts LE, "Breast Ultrasonography: State of the Art," Radiology, vol. 268, pp. 642–659, 2013. [PubMed: 23970509]

[9]. Cosgrove D, Piscaglia F, Bamber J, Bojunga J, Correas JM, Gilja OH, Klauser AS, Sporea I, Calliada F, Cantisani V, et al., "EFSUMB Guidelines and Recommendations on the Clinical Use

of Ultrasound Elastography.Part 2: Clinical Applications," Ultraschall in Med, vol. 34, pp. 238–253, 2013. [PubMed: 23605169]

[10]. Tanter M, Bercoff J, Athanasiou A, Deffieux T, Gennisson J-L, Montaldo G, Muller M, Tardivon A, and Fink M, "Quantitative Assessment of Breast Lesion Viscoelasticity: Initial Clinical Results Using Supersonic Shear Imaging," Ultrasound Med. Biol, vol. 34, pp. 1373–1386, 2008. [PubMed: 18395961]

[11]. Sarvazyan AP, Urban MW, and Greenleaf JF, "Acoustic Waves in Medical Imaging and Diagnostics," Ultrasound Med. Biol, vol. 39, pp. 1133–1146, 2013. [PubMed: 23643056]

[12]. Sarvazyan AP, Rudenko OV, Swanson SD, Fowlkes JB, and Emelianov SY, "Shear wave elasticity imaging: a new ultrasonic technology of medical diagnostics," Ultrasound Med. Biol, vol. 24, pp. 1419–1435, 1998. [PubMed: 10385964]

[13]. Bercoff J, Tanter M, and Fink M, "Supersonic shear imaging: a new technique for soft tissue elasticity mapping," IEEE Trans. Ultrason. Ferroelectr. Freq. Control, vol. 51, pp. 396–409, 2004. [PubMed: 15139541]

[14]. Nightingale K, Soo MS, Nightingale R, and Trahey G, "Acoustic radiation force impulse imaging: in vivo demonstration of clinical feasibility," Ultrasound Med. Biol, vol. 28, pp. 227–235, 2002. [PubMed: 11937286]

[15]. Song P, Zhao H, Manduca A, Urban MW, Greenleaf JF, and Chen S, "Comb-push ultrasound shear elastography (CUSE): a novel method for two-dimensional shear elasticity imaging of soft tissues," IEEE Trans. Med. Imaging, vol. 31, pp. 1821–1832, 2012. [PubMed: 22736690]

[16]. Yoon H, Aglyamov SR, and Emelianov SY, "Dual-Phase Transmit Focusing for Multiangle Compound Shear-Wave Elasticity Imaging," IEEE Trans. Ultrason., Ferroelect., Freq. Control, vol. 64, pp. 14391449, 2017.

[17]. Wang J-W, Guo Z-X, Lin Q-G, Zheng W, Zhuang S-L, Lin S-Y, Li A-H, and Pei X-Q, "Ultrasound elastography as an imaging biomarker for detection of early tumor response to chemotherapy in a murine breast cancer model: a feasibility study," Br. J. Radiol, vol. 91, p. 20170698, 2018.

[18]. Xu M and Wang LV, "Photoacoustic imaging in biomedicine," Rev. Sci. Instrum, vol. 77, p. 041101, 2006.

[19]. Beard P, "Biomedical photoacoustic imaging," Interface Focus, 2011.

[20]. Toi M, Asao Y, Matsumoto Y, Sekiguchi H, Yoshikawa A, Takada M, Kataoka M, Endo T, Kawaguchi-Sakita N, Kawashima M, et al., "Visualization of tumor-related blood vessels in human breast by photoacoustic imaging system with a hemispherical detector array," Sci. Rep, vol. 7, p. 41970, 2017. [PubMed: 28169313]

[21]. Vaupel P and Mayer A, "Hypoxia in cancer: significance and impact on clinical outcome," Cancer Metastasis Rev, vol. 26, pp. 225–239, 2007. [PubMed: 17440684]

[22]. Höckel M and Vaupel P, "Tumor Hypoxia: Definitions and Current Clinical, Biologic, and Molecular Aspects," Journal of the National Cancer Institute, vol. 93, pp. 266–276, 2001. [PubMed: 11181773]

[23]. Zhang HF, Maslov K, Sivaramakrishnan M, Stoica G, and Wang LV, "Imaging of hemoglobin oxygen saturation variations in single vessels in vivo using photoacoustic microscopy," Appl. Phys. Lett, vol. 90, p. 053901, 2007.

[24]. Mallidi S, Watanabe K, Timerman D, Schoenfeld D, and Hasan T, "Prediction of Tumor Recurrence and Therapy Monitoring Using Ultrasound-Guided Photoacoustic Imaging," Theranostics, vol. 5, pp. 289–301, 2015. [PubMed: 25553116]

[25]. Luke GP and Emelianov SY, "Label-free Detection of Lymph Node Metastases with US-guided Functional Photoacoustic Imaging," Radiology, vol. 277, pp. 435–442, 2015. [PubMed: 25997030]

[26]. Meng-Lin L, Jung-Taek O, Xie X, Ku G, Wei W, Chun L, Lungu G, Stoica G, and Wang LV, "Simultaneous Molecular and Hypoxia Imaging of Brain Tumors In Vivo Using Spectroscopic Photoacoustic Tomography," Proceedings of the IEEE, vol. 96, pp. 481–489, 2008.

[27]. Ferrara K, Pollard R, and Borden M, "Ultrasound Microbubble Contrast Agents: Fundamentals and Application to Gene and Drug Delivery," Annu. Rev. Biomed. Eng, vol. 9, pp. 415–447, 2007. [PubMed: 17651012]

[28]. Martin KH and Dayton PA, "Current status and prospects for microbubbles in ultrasound theranostics," Wiley Interdiscipl. Rev. Nanomed. Nanobiotechnol, vol. 5, pp. 329–345, 2013.

[29]. Sheeran PS and Dayton PA, "Phase-Change Contrast Agents for Imaging and Therapy," Curr. Pharm. Des, vol. 18, pp. 2152–2165, 2012. [PubMed: 22352770]

[30]. Wilson K, Homan K, and Emelianov S, "Biomedical photoacoustics beyond thermal expansion using triggered nanodroplet vaporization for contrast-enhanced imaging," Nat. Commun, vol. 3, p. 618,2012. [PubMed: 22233628]

[31]. Lin S, Shah A, Hernández-Gil J, Stanziola A, Harriss BI, Matsunaga TO, Long N, Bamber J, and Tang M-X, "Optically and acoustically triggerable sub-micron phase-change contrast agents for enhanced photoacoustic and ultrasound imaging," Photoacoustics, vol. 6, pp. 26–36, 2017. [PubMed: 28507898]

[32]. Sheeran PS, Luois S, Mullin L, Matsunaga TO, and Dayton PA, "Design of Ultrasonically-Activatable Nanoparticles using Low Boiling Point Perfluorocarbons," Biomaterials, vol. 33, pp. 3262–3269, 2012. [PubMed: 22289265]

[33]. Luke GP, Hannah AS, and Emelianov SY, "Super-resolution ultrasound imaging in vivo with transient laser-activated nanodroplets," Nano Lett,2016.

[34]. Yoon H, Yarmoska SK, Hannah AS, Yoon C, Hallam KA, and Emelianov SY, "Contrast-enhanced ultrasound imaging in vivo with laser-activated nanodroplets," Med. Phys, vol. 44, pp. 3444–3449, 2017. [PubMed: 28391597]

[35]. Yoon H, Hallam KA, Yoon C, and Emelianov SY, "Super-resolution imaging with ultrafast ultrasound imaging of optically triggered perfluorohexane nanodroplets," IEEE Trans. Ultrason., Ferroelect., Freq. Control,pp. 1–1, 2018.

[36]. Yoon H and Emelianov S, "Combined multi-wavelength photoacoustic and plane-wave ultrasound imaging for probing dynamic phase-change contrast agents," IEEE Trans. Biomed. Eng,pp. 1–1, 2018.

[37]. Emelianov SY, Aglyamov SR, Shah J, Sethuraman S, Scott WG, Schmitt R, Motamedi M, Karpiouk A, and Oraevsky AA, "Combined ultrasound, optoacoustic, and elasticity imaging," in Proc. SPIE, Photons Plus Ultrasound: Imaging and Sensing, 2004, p. 12.

[38]. Nguyen MN, Ding X, Yu J, Park D, Yu F, and Kim K, "Tri-modality Ultrasound Imaging System: Design and Phantom Experiment Results," in Proc. IEEE Int. Ultrason. Symp., 2014, pp. 325–328.

[39]. Montaldo G, Tanter M, Bercoff J, Benech N, and Fink M, "Coherent plane-wave compounding for very high frame rate ultrasonography and transient elastography," IEEE Trans. Ultrason. Ferroelectr. Freq. Control, vol. 56, pp. 489–506, 2009. [PubMed: 19411209]

[40]. FDA. (2008). Guidance for Industry and FDA Staff Information for Manufacturers Seeking Marketing Clearance of Diagnostic Ultrasound Systems and Transducers. Available: http://www.fda.gov/RegulatoryInformation/Guidances/ucm070856.htm

[41]. Loupas T, Peterson RB, and Gill RW, "Experimental evaluation of velocity and power estimation for ultrasound blood flow imaging, by means of a two-dimensional autocorrelation approach," IEEE Trans. Ultrason., Ferroelect., Freq. Control, vol. 42, pp. 689–699, 1995.

[42]. Song P, Manduca A, Zhao H, Urban MW, Greenleaf JF, and Chen S, "Fast shear compounding using robust 2-D shear wave speed calculation and multi-directional filtering," Ultrasound Med. Biol, vol. 40, pp. 1343–1355, 2014. [PubMed: 24613636]

[43]. Hall TJ, Bilgen M, Insana MF, and Krouskop TA, "Phantom materials for elastography," IEEE Trans. Ultrason., Ferroelect., Freq. Control, vol. 44, pp. 1355–1365, 1997.

[44]. Rouze NC, Wang MH, Palmeri ML, and Nightingale KR, "Parameters affecting the resolution and accuracy of 2-D quantitative shear wave images," IEEE Trans. Ultrason., Ferroelect., Freq. Control, vol. 59, pp. 1729–1740, 2012.

[45]. Ntziachristos V, "Going deeper than microscopy: the optical imaging frontier in biology," Nat. Methods, vol. 7, p. 603,2010. [PubMed: 20676081]

[46]. Yoon H, Luke GP, and Emelianov SY, "Impact of depth-dependent optical attenuation on wavelength selection for spectroscopic photoacoustic imaging," Photoacoustics, vol. 12, pp. 46–54, 2018. [PubMed: 30364441]

Author Manuscript Author Manuscript Author Manuscript Author Manuscript

[47]. Palmeri ML and Nightingale KR, "What challenges must be overcome before ultrasound elasticity imaging is ready for the clinic?," Imaging Med, vol. 3, pp. 433–444, 2011. [PubMed: 22171226]

[48]. Bamber J, Cosgrove D, Dietrich CF, Fromageau J, Bojunga J, Calliada F, Cantisani V, Correas JM, D'Onofrio M, Drakonaki EE, et al., "EFSUMB guidelines and recommendations on the clinical use of ultrasound elastography. Part 1: basic principles and technology," Ultraschall Med, vol. 34, pp. 169–184, 2013. [PubMed: 23558397]

[49]. Denis M, Mehrmohammadi M, Song P, Meixner DD, Fazzio RT, Pruthi S, Whaley DH, Chen S, Fatemi M, and Alizad A, "Combpush ultrasound shear elastography of breast masses: initial results show promise," PloS One, vol. 10, pp. e0119398-e0119398, 2015.

[50]. Chamming's F, Le-Frère-Belda M-A, Latorre-Ossa H, Fitoussi V, Redheuil A, Assayag F, Pidial L, Gennisson J-L, Tanter M, Cuénod C-A, et al., "Supersonic Shear Wave Elastography of Response to Anti-cancer Therapy in a Xenograft Tumor Model," Ultrasound Med. Biol, vol. 42, pp. 924–930, 2016. [PubMed: 26746382]

[51]. Rich LJ and Seshadri M, "Photoacoustic monitoring of tumor and normal tissue response to radiation," Sci. Rep, vol. 6, p. 21237, 2016. [PubMed: 26883660]

[52]. Dima A and Ntziachristos V, "In-vivo handheld optoacoustic tomography of the human thyroid," Photoacoustics, vol. 4, pp. 65–69, 2016. [PubMed: 27766210]

[53]. Deán-Ben XL, Merčep E, and Razansky D, "Hybrid-array-based optoacoustic and ultrasound (OPUS) imaging of biological tissues," Appl. Phys. Lett, vol. 110, p. 203703, 2017.

[54]. Fehm TF, Deán-Ben XL, and Razansky D, "Four dimensional hybrid ultrasound and optoacoustic imaging via passive element optical excitation in a hand-held probe," Appl. Phys. Lett, vol. 105, p. 173505, 2014.

[55]. Landa FJO, Deán-Ben XL, Sroka R, and Razansky D, "Volumetric Optoacoustic Temperature Mapping in Photothermal Therapy," Sci. Rep, vol. 7, p. 9695, 2017. [PubMed: 28851968]
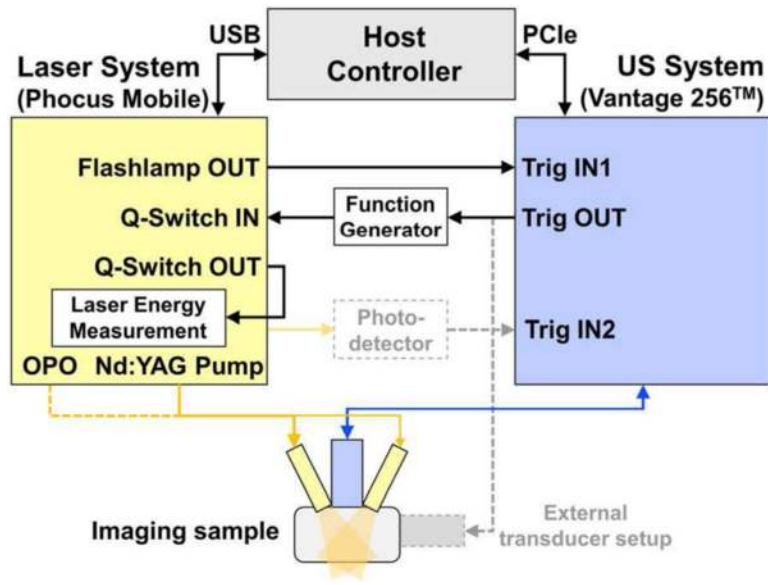
Fig. 1.
Block diagram of an overall imaging set-up with integrated ultrasound and laser systems.
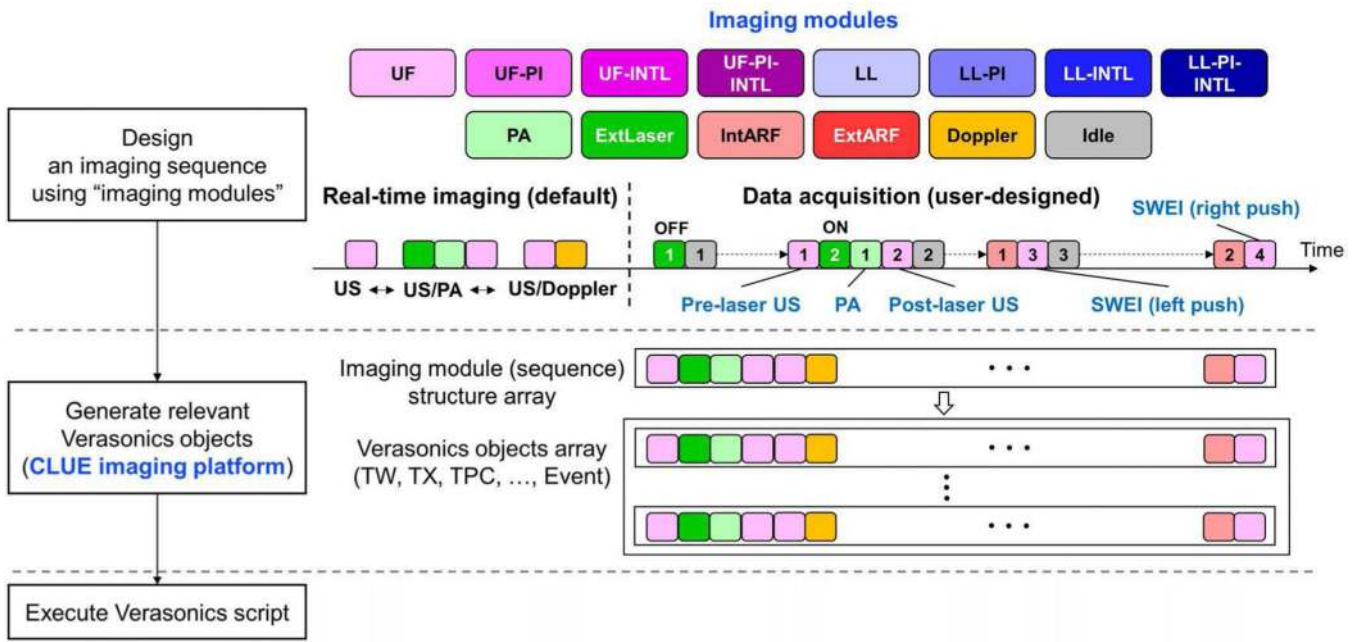
Fig. 2.
Design and execution process of an imaging sequence using the CLUE imaging platform.
All imaging modules here are uniquely color-coded for better visualization of them for the
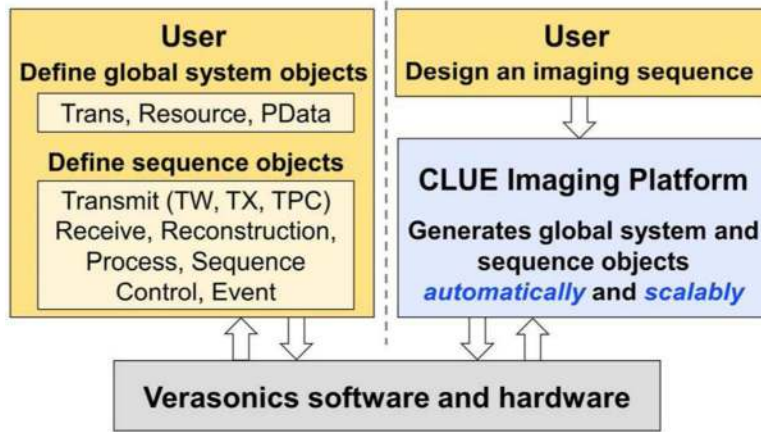rest of the paper.

Fig. 3.
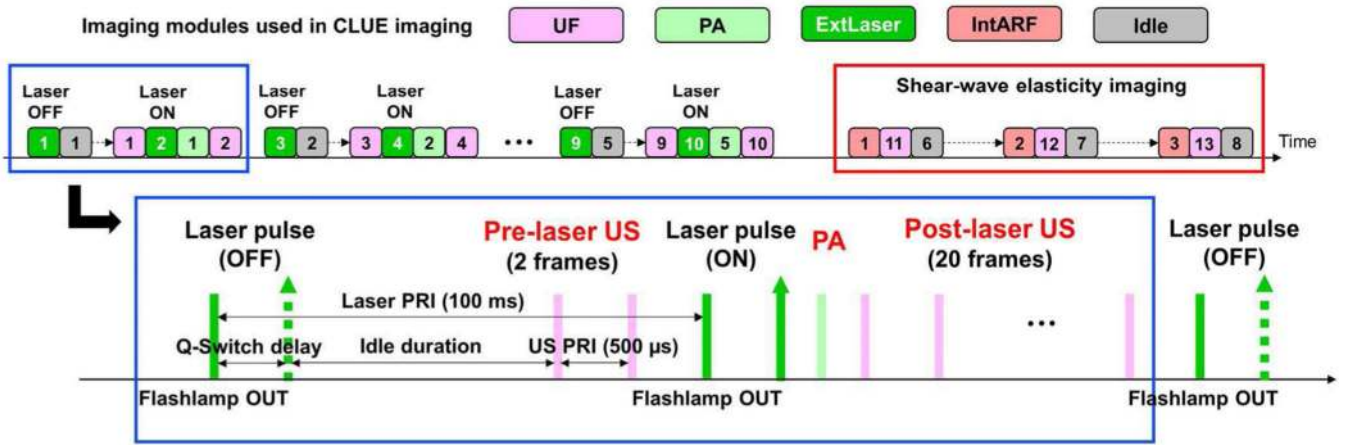A diagram showing the role of the CLUE imaging platform in interfacing users and Verasonics software and hardware.

Fig. 4.
A proposed CLUE imaging sequence including 5 sets of pre-laser US, PA, and post-laser US imaging sequences (blue rectangle) as a function of optical fluence and three sets of SWEI sequences (red rectangle). Two pre-laser US, one PA, and 20 post-laser US images were repeatedly and serially acquired with increasing optical fluence.
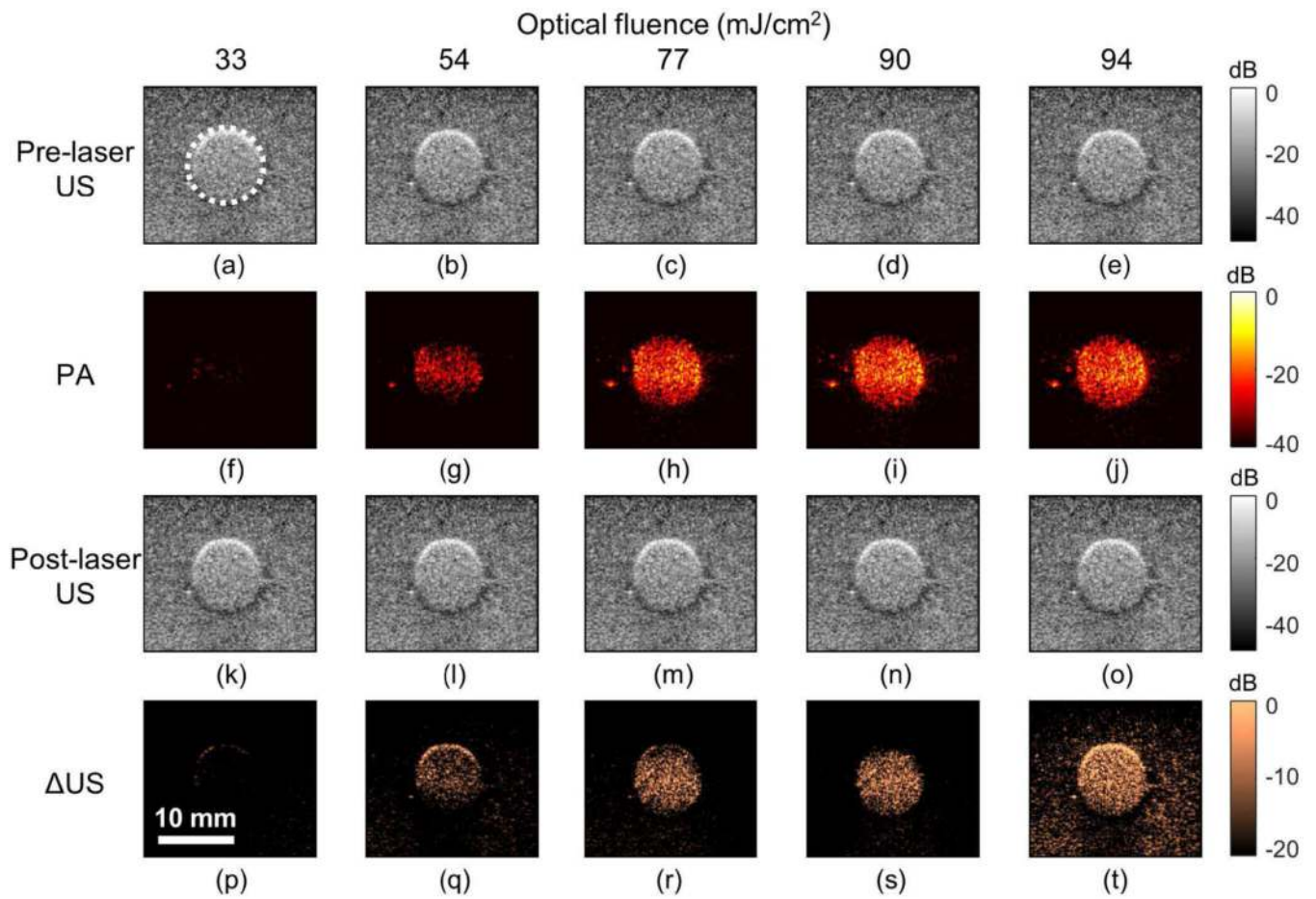
Fig. 5.
Processed pre-laser US, PA, post-laser US, and US images as a function of optical fluence obtained from the tissue-mimicking gelatin phantom.
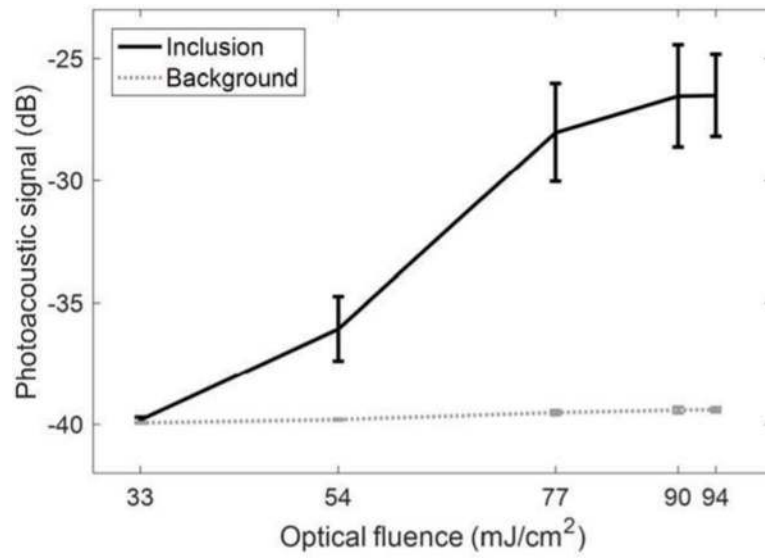
Fig. 6.
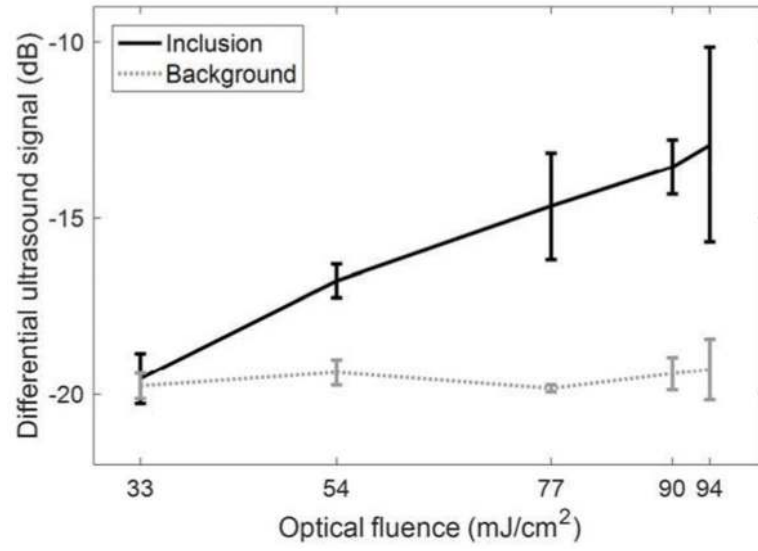Means and SDs of PA signals obtained inside and outside of the inclusion as a function of optical fluence.

Fig. 7.
Means and SDs of US signals obtained inside and outside of the inclusion as a function of optical fluence.
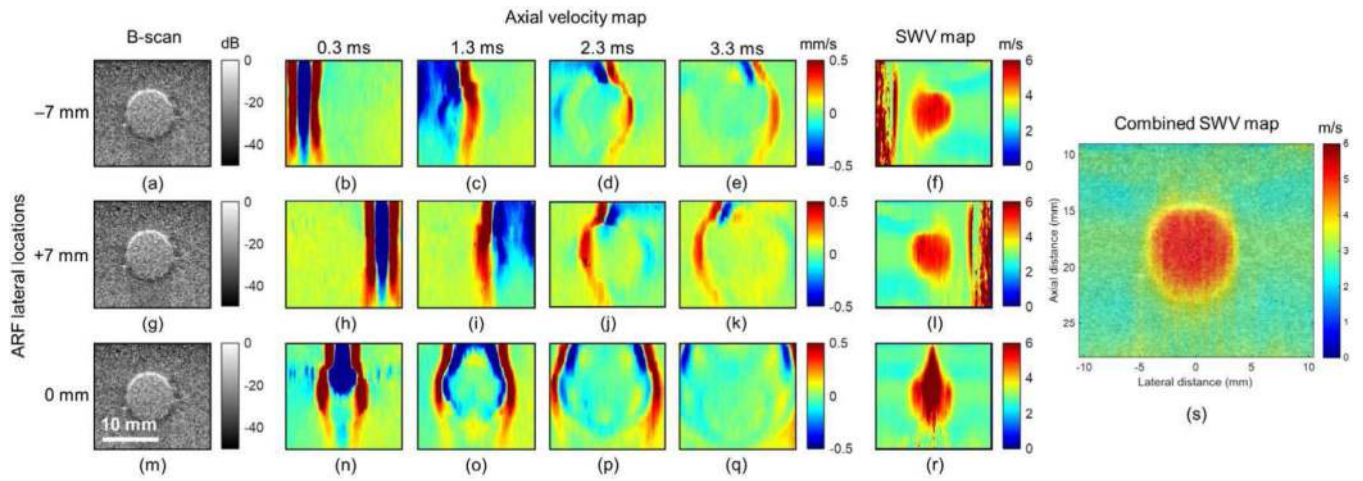
Fig. 8.
Estimated axial velocity sequences visualizing the propagation of the shear waves generated at three lateral locations in the gelatin phantom and three corresponding SWV maps.
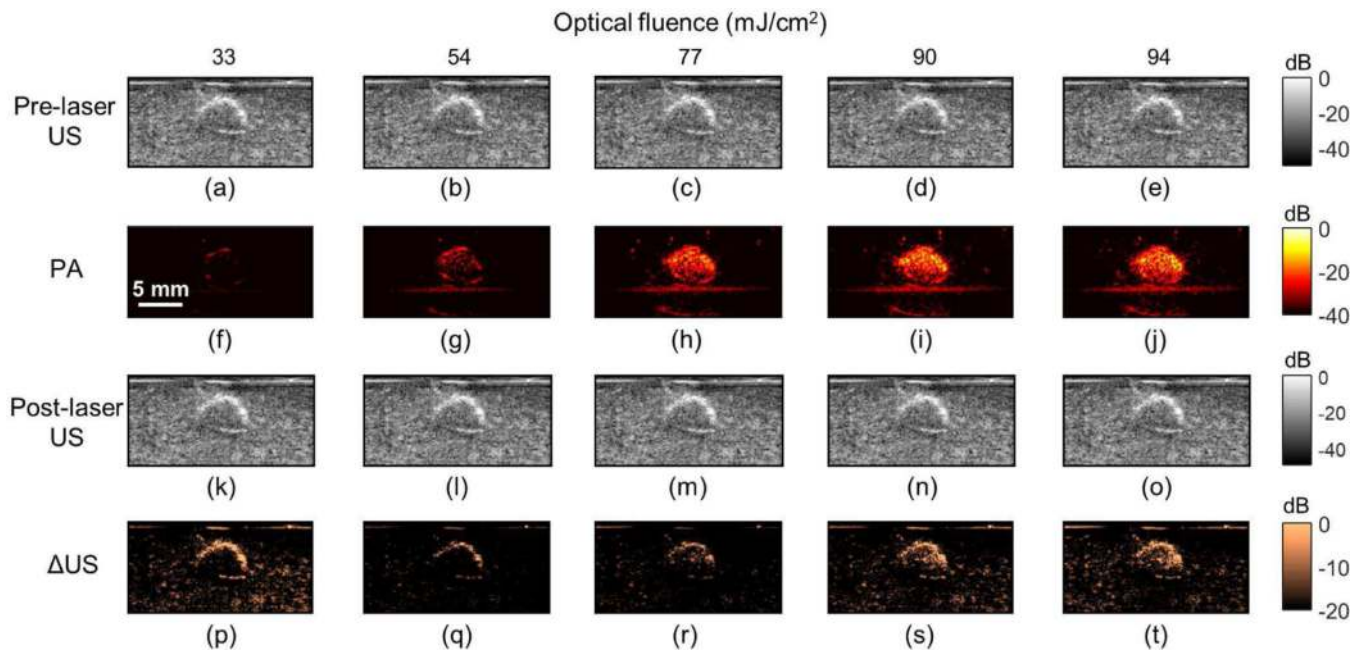
Fig. 9.
Processed pre-laser US, PA, post-laser US, and ΔUS images as a function of optical fluence. The images were obtained from the *ex vivo* mouse spleen embedded in gelatin phantom.
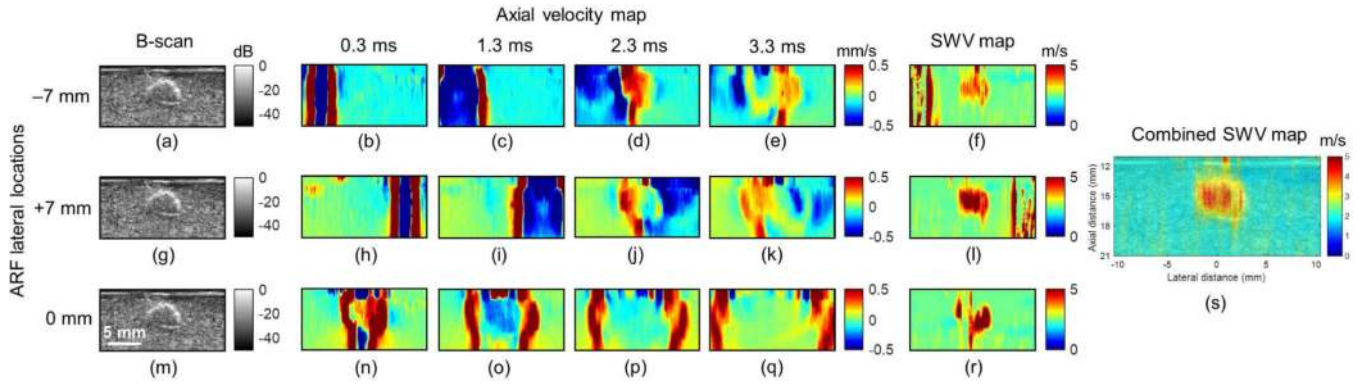
Fig. 10.
Estimated axial velocity sequences visualizing the propagation of the shear waves generated at three lateral locations in the phantom embedding the *ex vivo* mouse spleen and three corresponding SWV maps.

TABLE I

IMAGING MODULES USED IN CLUE IMAGING PLATFORM

Module name	Description
UF	Ultrafast imaging
UF-PI	Ultrafast pulse inversion imaging
UF-INTL	Ultrafast interleaved imaging
UF-PI-INTL	Ultrafast pulse inversion interleaved imaging
LL	Line-by-line imaging
LL-PI	Line-by-line pulse inversion imaging
LL-INTL	Line-by-line interleaved imaging
LL-PI-INTL	Line-by-line pulse inversion interleaved imaging
PA	Photoacoustic imaging
ExtLaser	Pulsed-laser excitation
IntARF	ARF excitation with an imaging transducer
ExtARF	ARF excitation with an external transducer
Doppler	Color/power Doppler imaging
Idle	Idle time delay (no operation)

TABLE II:

IMAGING PARAMETERS USED IN THE CLUE IMAGING SEQUENCE

	Ultrafast US and PA imaging of PFHnDs						SWEI		
	Laser pulsing (fake)	No operation	Pre-laser US	Laser pulsing (actual)	PA	Post-laser US	ARF	US tracking	No operation
Imaging module	ExtLaser	Idle	UF	ExtLaser	PA	UF	IntARF	UF	Idle
Module number	1,3,5,7,9	1,2,3,4,5	1,3,5,7,9	2,4,6,8,10	1,2,3,4,5	2,4,6,8,10	1,2,3	11,12,13	6,7,8
Wavelength	1064 nm			1064 nm					
Enable	False			True					
Q-Switch delay (μs)	400, 350, 300, 270, 250			400, 350, 300, 270, 250					
Idle duration		97.7 ms							500 ms
No. frames			2		1	20		120	
No. plane waves			1			1		3	
Sweeping angles			0°			0°		−2°, 0°, 2°	
PRI (1/PRF)	100 ms		500 μs	100 ms	250 μs	500 μs		100 μs	
Center frequency			8.9 MHz			8.9 MHz	6.5 MHz	8.9 MHz	
ARF lateral location (mm)							−7, 0, 7		
Focal depth							17.5 mm		
ARF duration							200 μs		
f-number							2.5		